

Potential diagenetic and detrital sources for calcareous sediments from the Carlsberg Ridge, Indian Ocean

Anil B. Valsangkar^{1,*}, D. V. Borole¹, Archana S. Shejwalkar²,
Niyati G. Kalangutkar¹, Nelita O. Fernandes³ and Cliffo C. Dias¹

¹National Institute of Oceanography, Dona Paula, Goa 403 004, India

²Present address: School of Earth and Ocean Sciences, University of Victoria, Victoria BC, Canada

³Present address: Directorate of Mines and Geology, Panaji, Goa 403 001, India

Six sediment cores from the Carlsberg Ridge (CR) were studied for elemental concentration, magnetic susceptibility (χ), grain size and clay mineral distribution, and sedimentation rate to decipher possible detrital and diagenetic contributions. The sediments were characterized by very low χ , moderate total organic carbon, high CaCO₃ content and high accumulation rate (3 cm/ kyr). Clay mineralogical and geochemical data suggest major continental source from the Arabian Sea, and very low Mn distribution, absence of tephra and characteristic magnetic signatures rule out volcanic or hydrothermal input. Consistent peaks around 10, 25, 45, 60 and 80 cm depth and high uranium are due to sedimentary diagenesis.

Keywords: Diagenesis, elemental concentration, magnetic susceptibility, sedimentation rate.

THE Carlsberg Ridge (CR) in the Indian Ocean separates the Arabian Basin from the Somali Basin. The CR has a typical rough morphology with non-transform discontinuities similar to slow-spreading ridges like the northern portion of the Mid-Atlantic Ridge (MAR). Previous studies¹⁻⁵ on the CR have specified half-spreading rate varying between 1.2 and 1.5 cm/yr, and the sub-bottom profiler records indicate the presence of isolated sediment cover only in the NW part of the CR. Although some studies⁶ have considered the possibility of hydrothermal activity along the CR to explain higher concentrations of Cu and Ni in the Arabian Sea sediments, there is no direct evidence. Unlike the Pacific and Atlantic Oceans^{7,8}, the CR sediments are not metalliferous, and are devoid of sulphide minerals.

In a recent cruise to the CR, an unusually large event plume was encountered^{9,10}, indicating sporadic volcanic and tectonic activity along the slow-spreading CR causing cataclysmic release of hydrothermal fluids. However, our attempts during the SK-207 cruise did not show such anomalous results¹¹ and suggested no hydrothermal input

in the area. During surveys by the National Institute of Oceanography (NIO), ~120 km NW section of the CR was mapped using multi-beam bathymetry system, where upper mantle and lower crustal rocks were recovered¹². Here we discuss the presence of diagenetic and detrital signatures in the sediments from the axial valley and flank regions of the CR using new geochemical, radiochemical, clay mineralogical and magnetic susceptibility data, and present the sedimentation rates.

Methodology

Sampling techniques

In a small portion out of the 440 km long section, a small segment of axial valley and flank region of NW CR in the Indian Ocean encloses thick sediments, from where six sediment cores were collected using spade and gravity corer (Figure 1) during SK-114 and SK-154 of *ORV Sagar Kanya* cruises. Spade core sediments (SPC-01 and

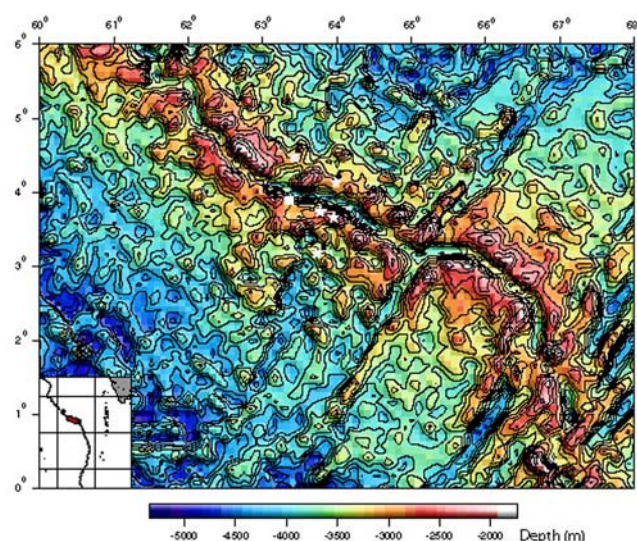


Figure 1. Sample locations in axial valley and flank region of Carlsberg Ridge with bathymetry contours. 1 = SPC-01, 2 = SPC-02, 3 = GC-03, 4 = GC-04, 5 = GC-05 and 6 = GC-06.

*For correspondence. (e-mail: vals@nio.org)

Table 1. ^{230}Th isotopes in SK-154, GC-04 core sediments

Depth (cm)	CaCO ₃ %	^{238}U (dpm/g)	^{234}U (dpm/g)	^{232}Th (dpm/g)	^{230}Th (dpm/g)	$^{230}\text{Th}_{\text{exc}}$ (dpm/g)
0–2	32.3	0.39 ± 0.01	0.63 ± 0.01	0.46 ± 0.04	8.87 ± 0.37	8.24 ± 0.37
4–6	37.3	1.12 ± 0.02	1.52 ± 0.03	0.69 ± 0.06	11.04 ± 0.51	9.51 ± 0.51
30–32	49.0	0.51 ± 0.01	0.64 ± 0.01	0.63 ± 0.05	9.75 ± 0.33	9.11 ± 0.33
40–42	53.6	0.79 ± 0.01	1.09 ± 0.02	1.10 ± 0.10	12.57 ± 0.58	11.48 ± 0.58
55–60	24.2	1.98 ± 0.04	3.45 ± 0.07	0.37 ± 0.04	4.11 ± 0.21	0.67 ± 0.22
68–70	48.2	0.85 ± 0.02	0.82 ± 0.02	1.12 ± 0.11	9.19 ± 0.48	8.38 ± 0.48
95–100	38.6	0.80 ± 0.02	1.36 ± 0.03	1.04 ± 0.08	6.95 ± 0.29	5.59 ± 0.29
108–110	44.8	1.01 ± 0.02	1.47 ± 0.03	1.14 ± 0.07	7.19 ± 0.25	5.72 ± 0.26
120–125	43.9	1.22 ± 0.02	0.76 ± 0.01	1.53 ± 0.14	7.55 ± 0.39	6.79 ± 0.39
122–125	42.6	0.75 ± 0.01	1.05 ± 0.02	1.20 ± 0.14	7.28 ± 0.47	6.23 ± 0.47

0.75 dpm = 1 ppm for ^{238}U ; 0.242 dpm = 1 ppm for ^{232}Th .

SPC-02) of SK-114 were sub-sectioned @ 2 cm interval up to 10 cm and then @ 5 cm up to the end, whereas four gravity cores (GC-03, GC-04, GC-05 and GC-06) from SK-154 were sub-sectioned @ 2 cm interval from top to the end of the core.

Grain size and clay mineralogy

Sediment texture was determined by the standard pipette analysis¹³ and oriented slides of 2 μm size clay fractions were made using 1 ml of treated sample for X-ray diffraction measurements carried out on Philips X-ray diffractometer (PW 1840) with Ni-filtered $\text{CuK}\alpha$ radiation, from 3° to 22° 2 θ /min, operated at 20 mA and 40 kV. Percentage of clay minerals was determined by weighted peak area method¹⁴. Total organic carbon (TOC) was estimated by following the wet oxidation method¹⁵ with dichromate. CaCO₃ % was determined using CO₂ Coulometer of UIC Inc., Model 5014. For this purpose, about 15–20 mg of the sample was used to acidify with 1 N HCl solution to liberate CO₂. The accuracy was <0.1% and the precision was better than $\pm 5\%$.

Chemical composition

Transition metal concentration of Fe and Mn by XRF, and Si and Al by ICP-MS was determined at NGRI, Hyderabad. For precision and accuracy of the analysis, six internal and international standards (JP-1, NIM-P, JB-3, GSR-3, JSB-1 and JB-2) were included. To determine magnetic susceptibility (χ), sediment samples were filled in non-magnetic, plastic sample holders of 8 cc capacity and oven-dried at 40°C. Low-frequency mass-specific magnetic susceptibility (χ) of the samples was measured on a Bartington magnetic susceptibility meter (model MS2). After switching on the instrument, it was allowed to warm up for half an hour. The mass-specific magnetic susceptibility (χ_{f} , $10^{-8} \text{ m}^3 \text{ kg}^{-1}$) was calculated from the data obtained with the MS2 meter.

Radiochemical measurements

Uranium–thorium (U–Th) radiochemical separation and purification were carried out following the standard procedure¹⁶, and ^{232}Th decay method was employed for determination of sedimentation rates (Table 1). The ^{230}Th excess (i.e. portion of ^{230}Th not supported by the decay of ^{234}U in the sediments) was calculated by subtracting the ^{234}U from the total ^{230}Th activity, using the equation: $^{230}\text{Th}_{\text{exc}}$ (dpm/g) = ^{230}Th (dpm/g) – ^{234}U (dpm/g).

Results

The present study includes various results on the sub-sections up to 100 cm depth. Elemental results are presented here on carbonate free basis (cfb), unless, otherwise mentioned.

Axial valley sediments

Totally three cores were obtained from the axial valley during SK-114 (SPC-01) and SK-154 (GC-03 and GC-04) cruise. The relative abundance of clay minerals in SPC-01 sediments (clayey-silt) indicated that illite (23–40%) and chlorite (22–46%) were the most dominant minerals than smectite (6–38%) and kaolinite (13–20%). Smectite was the highest only in the top surface; otherwise, it was the lowest among others (Figure 2 a). Illite, kaolinite, clay (Figure 2 a), TOC and carbonate (Figure 3 a) displayed higher value peak at 8–10 cm depth. Sand (8–12%) decreased and clay (31–46%) increased with depth (Figure 2 a). Fe and Mn content also increased from 20 cm depth (Figure 3 a).

The GC-03 core sediments behaved similarly, where CaCO₃, TOC and illite increased with depth, and sand (7–3%), and smectite (39–4%) showed a decrease. Kaolinite and chlorite displayed large variation and mixed behaviour. Noticeable changes occurred at 50 to 54 cm depth, where smectite, kaolinite, chlorite, sand, clay and Mn

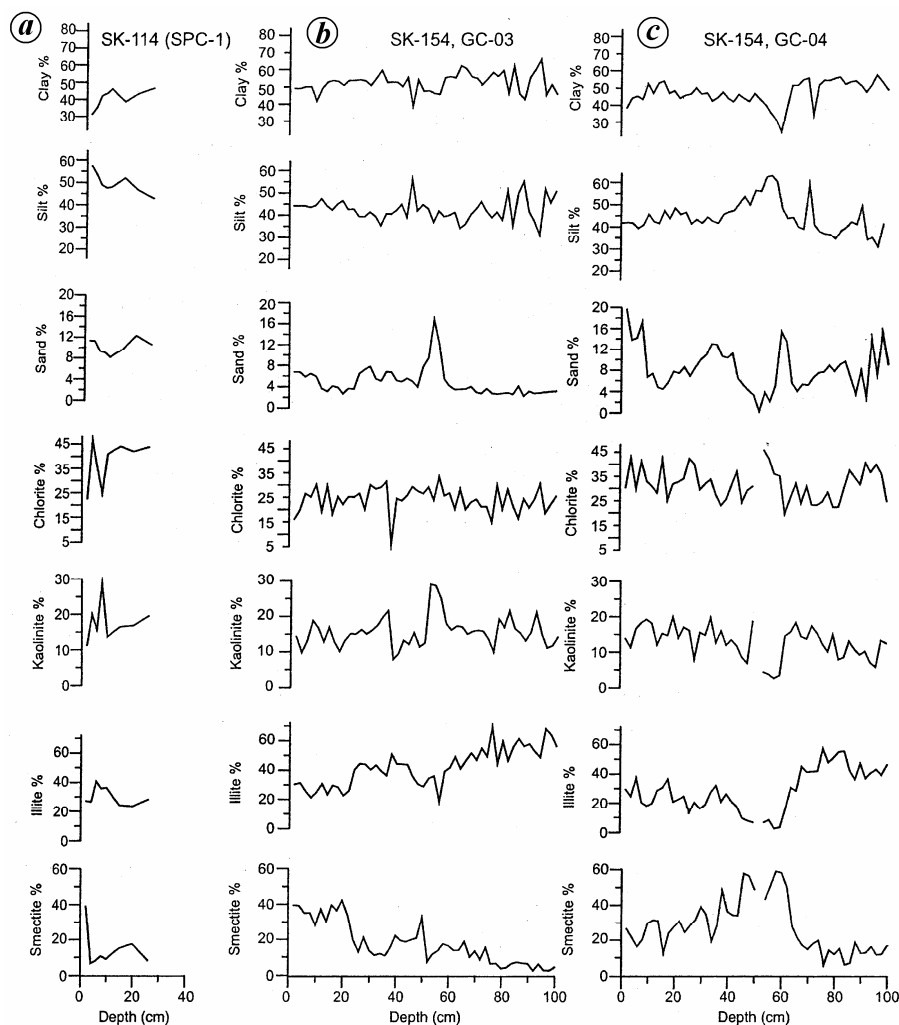


Figure 2 a-c. Profiles of clay minerals and sand-silt-clay content for SPC-01, GC-03 and GC-04 respectively.

were higher (Figure 2b) and CaCO_3 , TOC, Fe and susceptibility showed lower values (Figure 3b). Fe was higher at the surface (7.3%) and varied little with depth, and had small peaks at 26 and 42 cm depth (Figure 3b). Mn showed small increase from the surface to 48 cm depth, with small peaks at 24 and 46 cm, and then decreased to 0.06%. Susceptibility also showed small increase with depth (0.3–1.2 X_{lf}) and a break from 46 cm depth (Figure 3b). TOC was the highest (0.51%) at 80 cm depth.

The olive grey sediments of GC-04 exhibited distinct changes at 55–60 cm depth. Up to 50 cm depth, there was overall decrease in sand, illite, kaolinite and chlorite, and increase in clay and smectite content (Figure 2c). Carbonates declined sharply (53–14%) from 40 to 60 cm depth, where Mn, Fe and TOC had higher peak value, indicating lithological changes (Figure 3c). TOC and Fe values were constant up to 44 and 48 cm depth respectively, and then increased (Figure 3c). Mn displayed a peak at 10 and 50 cm depth. The silty-clay sediments had com-

paratively higher susceptibility value at the surface (1.6), which decreased down core to 0.36 X_{lf} with a change at 48–50 cm depth.

Flank sediments

Flank sediments include two cores from the north (SPC-02 and GC-05) and one from the south (GC-06). Illite and chlorite dominated the silty-clay sediments of SPC-02. The down-core profiles showed decrease in smectite, kaolinite, sand and silt content and increase in illite, chlorite and clay proportions (Figure 4a). Similarly, carbonates and Fe showed an increase, while Mn (0.6–0.1%) and TOC (0.3–0.1%) decreased (Figure 5a). Fe had a large range compared to Mn.

Silty-clay sediments of GC-05 exhibited similar down-core trends, where illite, chlorite and clay showed an increase, while smectite, kaolinite and sand decreased (Figure 4b). Fe had a wide range and decreased with depth up to 2%. Mn had a small peak around 22–40 cm, where Fe was

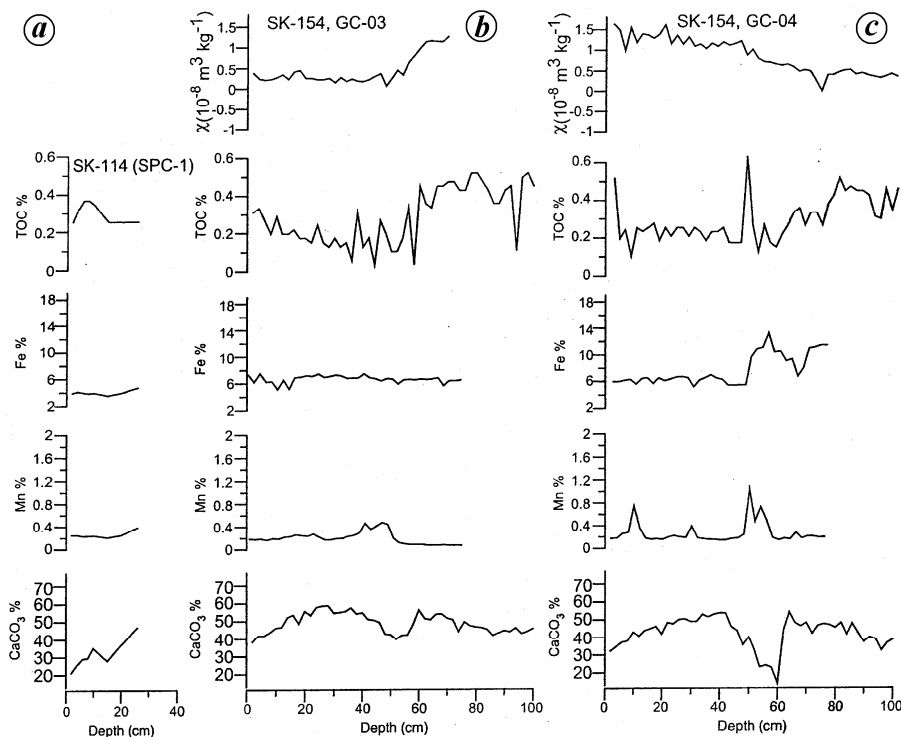


Figure 3 a-c. Profiles of carbonate, Mn, Fe, total organic carbon (TOC) and magnetic susceptibility (χ) for SPC-01, GC-03 and GC-04 respectively.

comparatively lower. Noticeable changes in carbonate, Mn, Fe and TOC content were marked from 50 to 60 cm depth (Figure 5b). TOC was noticeably high (0.4%) at 52 cm and magnetic susceptibility (MS) was maximum ($0.37 X_{if}$) at 48 cm depth.

GC-06 core sediments (SW flank) were silty-clay, where illite and clay showed a gradual increase, and others showed a down-core decrease (Figure 4c). MS decreased with increase in Fe with depth (Figure 5c). Higher Mn occurred for 36–56 cm sections, but noticeable changes were seen from 75 to 80 cm depth, where Fe, Mn and TOC content increased and CaCO_3 dropped to 48%. Similarly, higher peak value for carbonate and Mn, and lower peak value of Fe and TOC occurred at ~60 cm depth (Figure 5c).

All the cores had similar down-core trends for Si and Al (Figures 6 and 7 respectively), with peaks at around 6, 10, 14, 26, 33, 52 and 80 cm. Similarly, Mn/Al ratio had higher peak values at different depths (Figure 8). In most cores, the Mn/Al peak was seen around 40 cm depth. Variation in K content for axial valley sediment (1.3–3.9%) was comparatively smaller than that for the flank sediments (0.8–8.0%). Except for GC-05, the down-core profiles of all other cores showed an increase of K with depth (Figure 9).

U–Th dating

The decay curve up to 125 cm depth (excluding the 55 cm plot) appears to be linear (Figure 10). The estimated

sediment accumulation rate from $^{230}\text{Th}_{ex}$ decay profile for GC-04 core works out to be 3.03 ± 0.14 cm/kyr ($n = 11$; $r = -0.6$ and $P \leq 0.05$) for the top to 125 cm down core (11 samples, excluding the one at 55 cm). With this rate, the base of the core at 100 cm depth was estimated to be 33 kyr old.

Discussion

Source of CR sediments

Terrigenous source: The CR sediments are silty-clay throughout, except for the top 50–60 cm in the axial valley, where presence of both silty-clay and clayey-clay indicates mixing of the sediments (Table 2). Despite differential inputs, the Si and Al down-core profiles (Figures 6 and 7 respectively) are analogous and strongly imply a single (terrigenous) source for the CR sediments. The flank sediments of the CR are characterized by high illite (40–50%) and low smectite (<20%), whereas the axial valley sediments have comparatively low illite (30–40%) and high smectite clay (30–40%). Illite is most abundant clay mineral in the Indus River sediments and in the Iran-Makran soils¹⁷. Illite is also the dominant clay mineral in the northern Arabian Sea sediments, which has the highest concentrations in sediments in the areas between the Indus Fan and the Persian Gulf¹⁸. The ODP site 728 A in the NW Arabian Sea also has illite and chlorite as the most dominant clay minerals influenced by the terri-

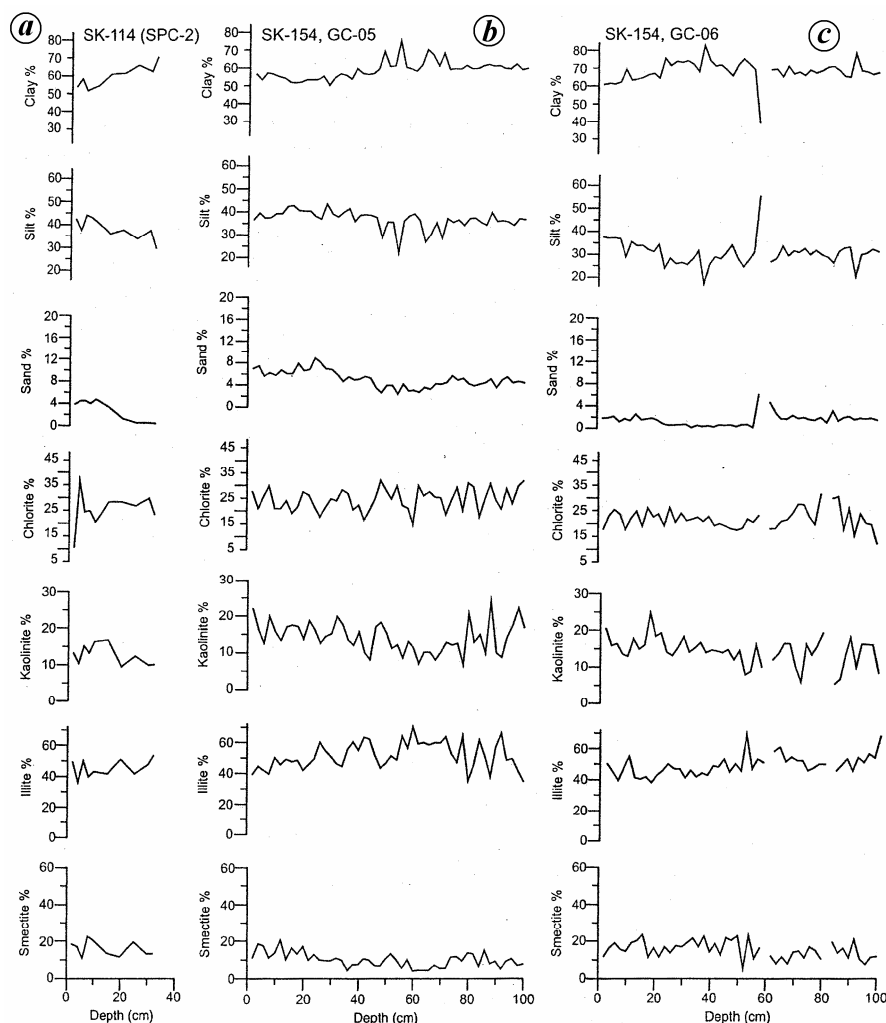


Figure 4a-c. Profiles of clay minerals and sand-silt-clay content for SPC-02, GC-05 and GC-06 respectively.

genous fractions¹⁹. The northwesterly wind system which was dominant during the Holocene, appears to be responsible for sediment transportation to the Arabian Sea²⁰. Therefore, high illite and chlorite (~20–30% in the axial valley and ~18–35% on the flanks) in the CR sediments strongly points towards Arabian Sea source, which in turn has a mixed source, predominantly from the Indus.

The supply of smectite clay to the Arabian Sea sediments from the Bay of Bengal²¹ or far from the southern latitudes below the equator due to melting of ice has been doubted by previous workers²². The Indus River originates in Tibet and follows the Indus Suture Zone through the Dras volcanics (island arc basalts and dacites) in the Himalayan mountain ranges and arid regions of Pakistan-India and drains to the Arabian Sea. The major source of smectite to the eastern Arabian Sea is from the Deccan Trap, whereas the Arabian Peninsula, Persian Gulf and Gulf of Oman have minor contribution of smectite in the western Arabian Sea¹⁹. The smectite abundance from 25°N to 5°N (close to the CR) in the Arabian Sea has been

reported¹⁷ to be constant or <20%. It is reported that the high smectite band (>40–50%) exist around 20°N in the Arabian Sea is due to dispersion of smectite by the Narmada and Tapti rivers towards west by the westward and northward currents and oceanic circulation¹⁷, and that the smectite from the rivers is not transported towards south as revealed from the decrease in smectite content (<10%) along the South Indian margin¹⁷. Therefore, it is opined that smectite (10–20% on the flanks) in the CR sediments is derived from the Arabian Sea (similar to illite) and not from the Indian margin. However, presence of high smectite (30–40%) in the axial valley further point towards an additional source, which appears remote due to the alteration of volcanic basalts in the absence of volcanic or hydrothermal activity in the CR. Therefore, the source of smectite for the axial valley sediments is the most likely from the African soil, brought to the CR by the northerly-bound equatorial currents, and the arid source¹⁹ is doubtful due to low crystallinity of the smectite clay.

The observed increase in K content with depth in almost all the sediment cores from the axial valley and flank

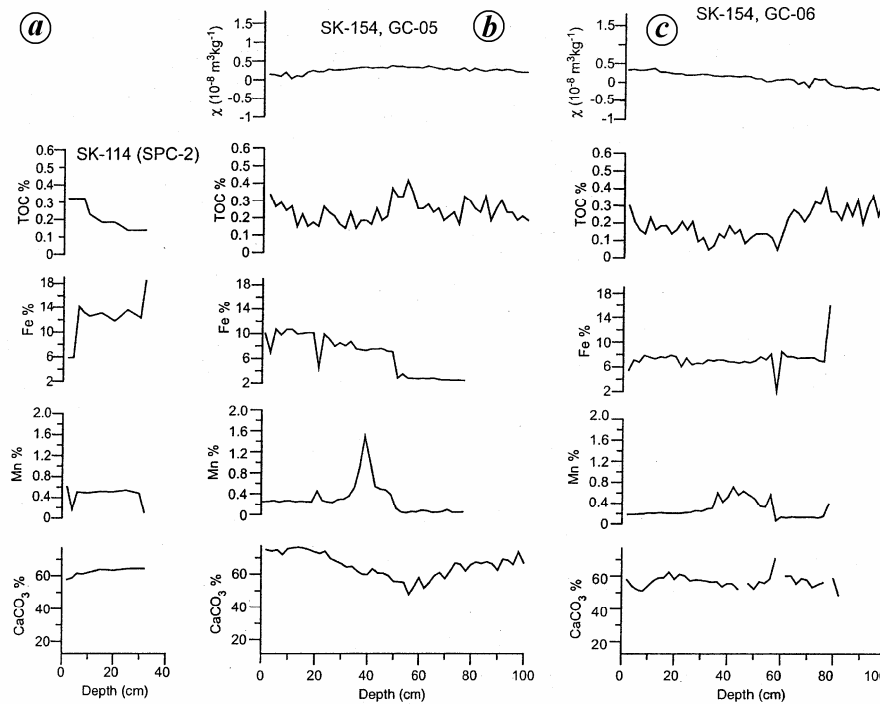


Figure 5 a-c. Profiles of carbonate, Mn, Fe, TOC and MS (χ) for SPC-02, GC-05 and GC-06 respectively.

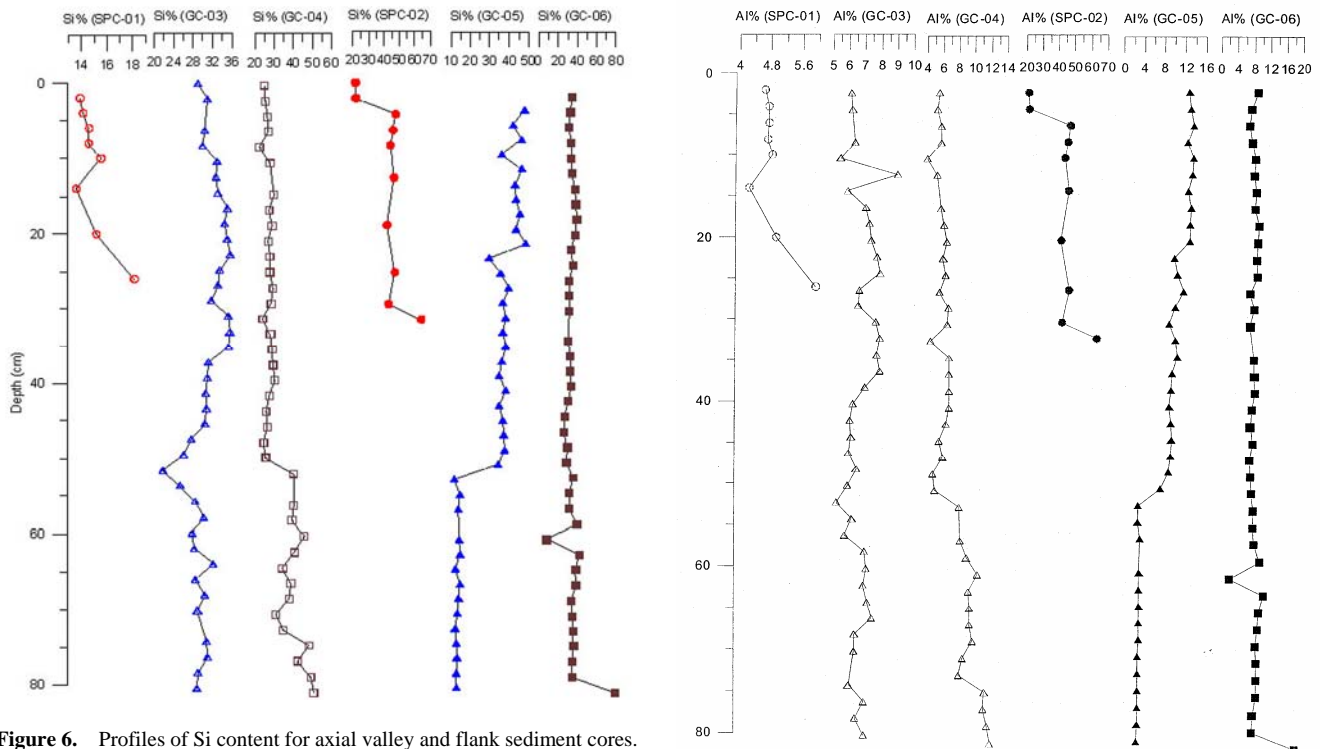


Figure 6. Profiles of Si content for axial valley and flank sediment cores.

Figure 7. Profiles of Al content for axial valley and flank sediment cores.

regions (Figure 9) suggests the larger detrital input for the deeper samples. Relatively high kaolinite (12–15% in the valley and 13–22% on flanks) is probably derived from the tropical soils of southern India and Africa–Madagascar due to northerly-bound equatorial circulation currents from south of the CR, as suggested earlier¹⁷.

Biogenic source

TOC variation in the sediments (0.3–0.5%) is normal and within the range of deep-sea sediments. The flank sedi-

ment cores were retrieved between 3700 and 4600 m water depths. The higher CaCO_3 (47–76%) in the flank sediments suggests no effect of dissolution of CaCO_3 and indicates deeper lysocline depth. The sediment cores from depth range 4300–4400 m in the axial valley have comparatively lower carbonates (17–58%), which shows an increase with depth (Figures 3 a–c) and supports deeper lysocline in the CR. The CR crest is known for high biological productivity and samples have high foraminiferal abundance. Higher carbonate content (>70%) in the flank sediments also indicates higher sedimentation rates in the area, and that high biological productivity and high sedimentation rates are responsible for high carbonate flux in the CR area, which is also acting as a strong diluent on the other elemental phase, as observed earlier²³.

Volcanic source

Magnetic fractions in sediments are normally derived from volcanic and terrigenous inputs, biogenic minerals and diagenetic alteration²⁴. Absence of tephra material (volcanic) in sand-sized fractions of the CR sediments clearly indicates absence of volcanic activity in the area. Absence of distinct susceptibility peaks in the down-core

profiles of all the sediment cores further suggests no volcanic or hydrothermal contribution from any nearby source. Both these indicators imply that the sediment source for the CR is non-volcanic.

Hydrothermal signatures

Enrichment of Mn is considered as one of the important hydrothermal signatures, as Mn could be incorporated either by diagenetic or hydrothermal source. Mn profiles for all the cores showed no significant enrichment in the top sediments (Figures 3 and 5), which behaved as normal pelagic sediments²⁵. Sharp peaks of Mn observed at different depths in all the cores appeared to be typical of oxidation fronts in diagenetic system^{26–28} and suggest that higher Mn may not be due to hydrothermal input and that diagenetic processes play a key role. Although Mn variation was low to moderate (0.06–1%) for valley sediments, the overall range was up to 0.5% and spikes of 0.7 and 1% were observed at a few depths (8–10, 50–52 and 56–58 cm, Figure 3 c) in GC-04 core sediments. Although Mn ranged from very low to moderately high values for flank sediments (0.03–1.5%), the actual range remained up to 0.6%, leaving spikes of >1% at 38 to 42 cm depth in

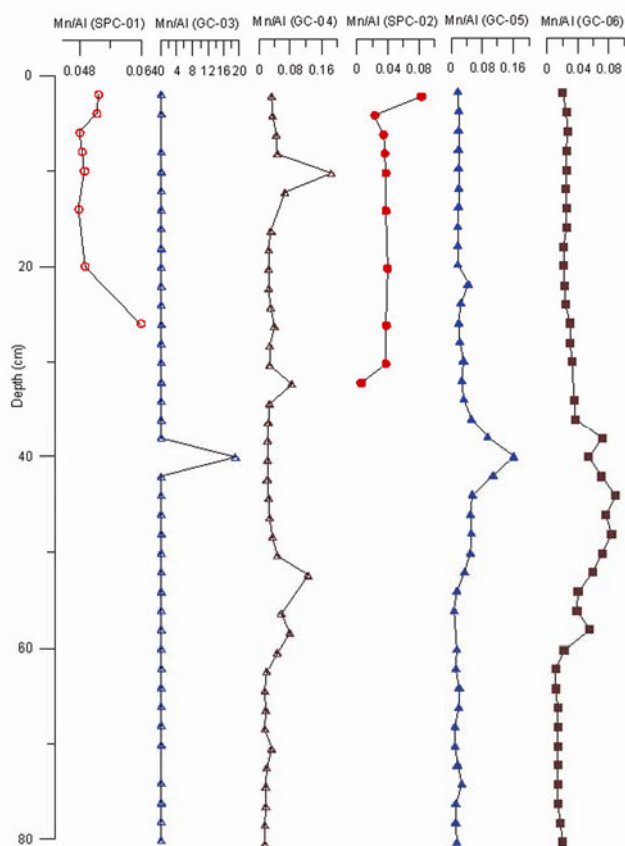


Figure 8. Profiles of Mn/Al ratio for axial valley and flank sediments.

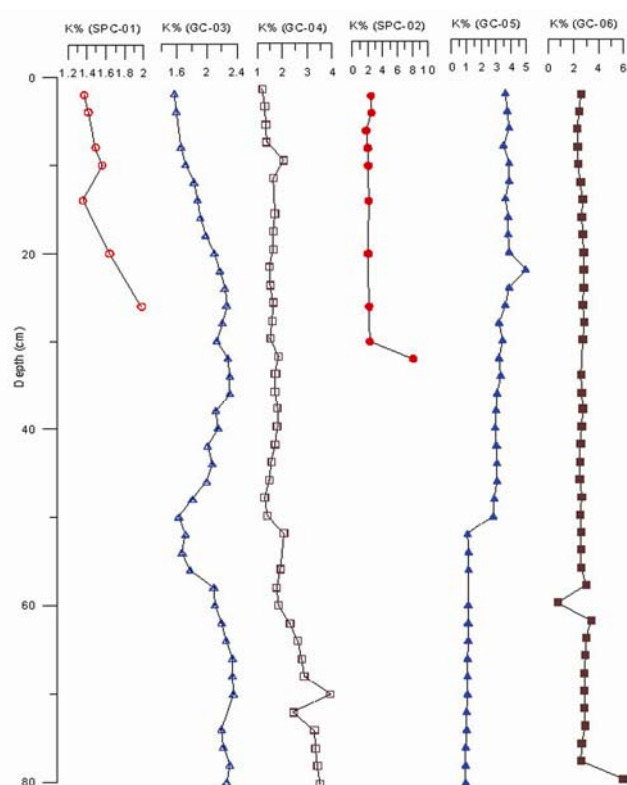


Figure 9. Profiles of K content for axial valley and flank sediments.

Table 2. Sediment texture and major clay minerals from Carlsberg Ridge

Location	Sample no.	Core depth (cm)	Sediment type	Major type sediment	Decreasing abundance of clay minerals
Axial valley	SK-114, SPC-1	0–20 20–26	Clayey-silt Silty-clay	Clayey-silt	0–2: SIKC 2–4: CIKS 4–8: ICKS 8–26: CIKS
Axial valley	SK-154, GC-03	0–44 44–46 45–80 80–82 82–86 86–88 88–94 94–96 96–98 98–100	Silty-clay Clayey-silt Silty-clay Clayey-silt Silty-clay Clayey-silt Silty-clay Clayey-silt Silty-clay Clayey-silt	Clayey-silt and Silty-clay	0–22: SICK 22–36: ICKS 36–50: ICSK 50–100: ICKS
Axial valley	SK-154, GC-04	0–2 2–16 16–18 18–20 20–22 22–32 32–34 34–38 38–62 62–70 70–72 72–90 90–92 92–100	Clayey-silt Silty-clay Clayey-silt Silty-clay Clayey-silt Silty-clay Clayey-silt Silty-clay Clayey-silt Silty-clay Clayey-silt Silty-clay Clayey-silt Silty-clay	0–38: Silty-clay 38–62: Clayey-silt 62–100: Silty-clay	0–8: CISK 8–28: CSIK 28–62: SCIK 62–100: ICSK
NW flank	SK-114, SPC-2	0–32	Silty-clay	Silty-clay	0–32: ICSK
NW flank	SK-154, GC-05	0–100	Silty-clay	Silty-clay	0–100: ICKS
SW flank	SK-154, GC-06	0–56 56–58 58–60 60–100	Silty-clay Clayey-silt No sample Silty-clay	Silty-clay	0–100: ICSK

S, Smectite; I, Illite; K, Kaolinite and C, chlorite.

Table 3. Inter-element relationship of axial valley sediments

	SPC-01; N = 8			GC-03; N = 35				GC-04; N = 38			
	Fe	Mn	TOC	Fe	Mn	TOC	MS	Fe	Mn	TOC	MS
Depth	0.45	0.62	-0.43	-0.08	-0.22	0.29	0.69	0.72	0.01	0.16	-0.90
Fe		0.95	0.47		0.23	-0.23	-0.25		0.26	0.02	0.75
Mn			0.58			0.25	-0.65			0.04	0.05
TOC			1.00				0.67				0.20
	$r = 0.67$, CL = 95%			$r = 0.33$, CL = 95%				$r = 0.32$, CL = 95%			

r = Correlation coefficient; CL = Confidence level.

GC-05 and 0.7% at 42–44 cm depth in GC-06 (Figure 5 *b* and *c* respectively). The ternary diagrams²⁹ show that the field occupied by the CR plots is close to that of the Pacific sediments (Figures 11 and 12) and strongly rule out the possibility of hydrothermal activity, which could be a possible cause for the Mn enrichment.

Diagenetic signatures

The CR sediments have dissimilar down-core MS profiles compared to Fe and Mn content (Figures 3 *b*, *c* and 5 *b*,

c), and inverse relationship between TOC and CaCO₃ (Figures 3 *a–c* and 5 *a–c*) suggesting diagenetic influence. In the absence of hydrothermal input in the CR, the observed strong correlation of Fe and Mn in SPC-01 (0.95, Table 3), or significant correlation in GC-05 (0.35, Table 4), and the sudden increase in Fe and Mn at ~26 cm depth in SPC-01 (Figure 3 *a*), at 45 cm depth in GC-04 (Figure 3 *c*), and at 80 cm depth in GC-06 (Figure 5 *c*) is possible due to strong diagenetic influence in the sediments. Most Mn peaks occurring at different depths in the CR sediments were sharp, which is typical of

Table 4. Inter-element relationship of flank sediments

	SPC-02; N = 10			GC-05; N = 39				GC-06; N = 39			
	Fe	Mn	TOC	Fe	Mn	TOC	MS	Fe	Mn	TOC	MS
Depth	0.68	-0.25	-0.95	-0.89	-0.27	0.21	0.67	0.24	0.02	0.33	-0.91
Fe		-0.19	-0.58		0.39	0.35	0.56		0.11	0.26	0.15
Mn			0.18			-0.26	0.11			-0.43	-0.03
TOC			1.00				0.14				0.18
	$r = 0.58, CL = 95\%$			$r = 0.31, CL = 95\%$				$r = 0.32, CL = 95\%$			

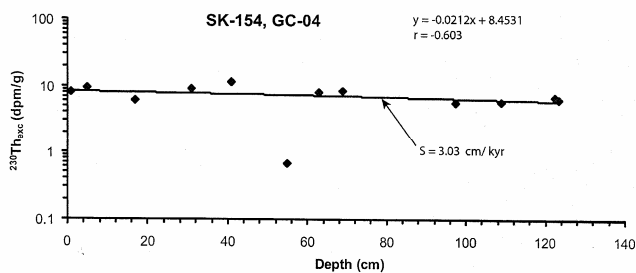


Figure 10. ^{230}Th ex profile for GC-04 sediment core showing sedimentation rate = 3.03 cm/kyr (excluding plot ~58 cm). Correlation (-0.6) is above the level of significance (0.55 for $n = 11$).

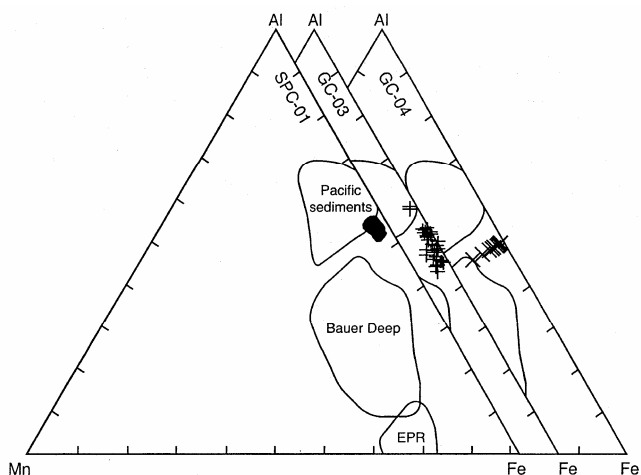


Figure 11. Ternary diagram of Al, Fe and Mn for axial valley sediment cores (SPC-01, GC-03 and GC-04). EPR, East Pacific Rise.

migration of oxidation front in a diagenetic system²⁸. Changes in Mn concentration of the sediments containing little organic matter is possible due to penetration of oxygen at depths³⁰. The CR sediments contained a small quantity (<0.6%) of TOC, and the down-core profiles for axial valley sediments showed an increase in Mn and decrease of TOC at about 15 cm depth in SPC-1 (Figure 3 a), indicating consumption of oxygen due to diagenesis. Similar inverse relation for Mn and TOC of GC-03 was observed at ~40 cm depth (Figure 3 b), and ~10 and 26 cm depth of GC-04 (Figure 3 c). However, increase in TOC, Mn and Fe at ~45 cm depth of GC-04 (Figure 3 c) may reflect oscillation of oxic-anoxic boundary layer due to pulsed sedimentation. The down-core profiles for flank

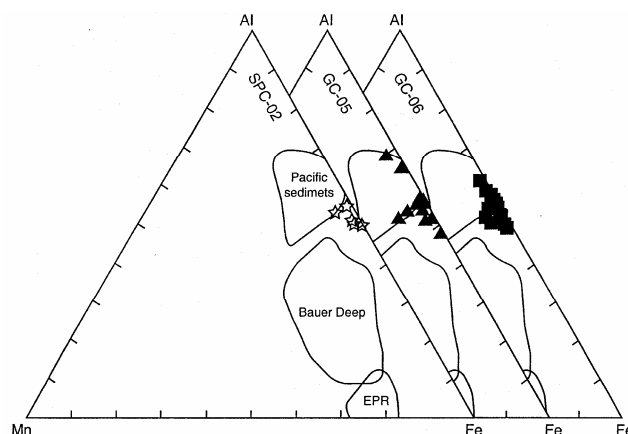


Figure 12. Ternary diagram of Al, Fe and Mn for sediment cores from flanks (SPC-02, GC-05 and GC-06).

sediments also showed an inverse relation of TOC and Mn in the surface sediments of SPC-2 (Figure 5 a), and displayed lower TOC value (<0.2%) for peak value of Mn (1.6%) at ~40 cm depth of GC-05 (Figure 5 b) and GC-06 (Figure 5 c). However, as observed for the axial valley, the increase in TOC, Mn and Fe at ~85 cm depth in GC-06 (Figure 5 c) for the flank sediments is due to non-diagenetic effects.

Possibility of winnowing of high U in samples representing jumps of TOC, Mn (Figures 3 a-c and 5 a-c) and sand (Figures 2 a-c and 4 a-c), particularly around 50 cm depth has been ruled out as ^{230}Th depth profile (Figure 10) showed no winnowing except for the one low ^{230}Th excess at 55 cm depth. Therefore, high U in the analysed samples indicates diagenetic mobilization of U and that the internal sedimentary diagenesis has given rise to consistent peaks at around 10, 25, 45, 60 and 80 cm depth.

Conclusion

Clay mineralogical, geochemical and U-Th isotopic studies of sediments from the CR showed that the major sediment sources are continental, biogenic and diagenetic. The illite-rich sediments had high accumulation rates (3 cm/kyr) and were typically characterized by low Mn, very low χ , moderate TOC and high carbonate content. Absence of Mn enrichment, very low MS and monotonous down-core profile in all the cores rule out volcanic

or hydrothermal contribution in the sampling area. The ^{230}Th depth profile showed no winnowing, and internal sedimentary diagenesis appeared responsible for U enrichment and consistent peaks at different depths.

1. Le Pichon, X. and Heirtzler, J. R., Magnetic anomalies in the Indian Ocean and sea-floor spreading. *J. Geophys. Res.*, 1968, **73**, 2101–2117.
2. McKenzie, D. P. and Slater, J. G., The evolution of the Indian Ocean since the Late Cretaceous. *Geophys. J. R. Astron. Soc.*, 1971, **25**, 437–528.
3. Ramana, V., Ramprasad, T., Kamesh Raju, K. A. and Desa, M., Geophysical studies over a segment of a Carlsberg Ridge, Indian Ocean. *Mar. Geol.*, 1993, **115**, 21–28.
4. Chaubey, A. K., Bhattacharya, G. C., Murty, G. P. S. and Desa, M., Spreading history of the Arabian Sea: some new constraints. *Mar. Geol.*, 1993, **112**, 343–352.
5. Kamesh Raju, K. A., Kodagali, V. N. and Fujimoto, H., In Proceedings of 35th Annual Convention of Indian Geophysical Union, National Institute of Oceanography, Goa, 1998, pp. 29–30.
6. Shankar, R., Subbarao, K. V. and Kolla, V., Geochemistry of surface sediments from the Arabian Sea. *Mar. Geol.*, 1987, **76**, 253–279.
7. Rona, P. A., Black smokers and massive sulfides at the TAG hydrothermal field, Mid-Atlantic Ridge 26°N (abs.). *EOS*, 1985, **66**, 936.
8. Minniti, M. and Bonavia, F. F., Copper-ore grade hydrothermal mineralization discovered in a seamount in the Tyrrhenian Sea (Mediterranean): is the mineralization related to porphyry-coppers or to base metal lodes? *Mar. Geol.*, 1984, **59**, 271–282.
9. Murton, B. J., Baker, E. T., Sands, C. M. and German, C. R., Detection of an unusually large hydrothermal event plume above the slow-spreading Carlsberg Ridge, NW Indian Ocean. *Geophys. Res. Lett.*, 2006, **33**, 1–5.
10. Anon., Cruise report of *RSS Charles Darwin* (CD-149) (18 July–6 August 2003), Southampton Oceanography Centre, UK, p. 3.
11. Anon., Cruise report of *ORV Sagar Kanya* (SK-207) (13 July–19 August 2004), National Institute of Oceanography, Dona Paula, Goa, p. 27.
12. Mudholkar, A. V., Kodagali, V. N., Kamesh Raju, K. A., Valsangkar, A. B., Ranade, G. H. and Ambre, N. V., Geomorphological and petrological observations along a segment of slow-spreading Carlsberg Ridge. *Curr. Sci.*, 2002, **8**, 982–989.
13. Folk, R. L., *Petrology of Sedimentary Rocks*. Hemphills, Austin, 1968, p. 177.
14. Byscaye, P. E., Mineralogy and sedimentation of recent deep sea clay in Atlantic Ocean and adjacent seas and oceans. *Geol. Soc. Am. Bull.*, 1965, **76**, 803–831.
15. El Wakeel and Riley, J. P., Determination of organic carbon in the marine muds. *J. Cons. Perm. Int. Explor. Mer.*, 1957, **22**, 180–183.
16. Krishnaswami, S. and Sarin, M. M., The simultaneous determination of Th, Pu, Ra isotopes ^{210}Pb , ^{55}Fe , ^{32}Si and ^{14}C in marine suspended phases. *Anal. Chim. Acta*, 1976, **83**, 171–181.
17. Kolla, V., Kostecki, J. A., Robinson, F., Biscaye, P. E. and Ray, P. K., Distributions and origins of clay minerals and quartz in surface sediments of the Arabian Sea. *J. Sediment. Petrol.*, 1981, **51**, 563–569.
18. Goldberg, E. D. and Griffin, J. J., The sediments of the northern Indian Ocean. *Deep Sea Res.*, 1970, **17**, 513–537.
19. Das, S. S., Maurya, A. S., Pandey, A. C., Bhan, U. and Rai, A. K., Influence of sediment source and monsoonal variations on the late Quaternary clay mineral assemblages at ODP site 728A, north-western Arabian Sea. *Curr. Sci.*, 2008, **95**, 1320–1326.
20. Sirocko, F. and Sarnthein, M., Wind-borne deposits in the north-western Indian Ocean: Record of Holocene sediments versus modern satellite data. In *Palaeoclimatology and Palaeometeorology: Modern and Past Patterns of Global Atmospheric Transport* (eds Leinen, M. and Sarnthein, M.), NATO ASI Series, 1989, vol. 282, pp. 401–433.
21. Nigam, R., Borole, D. V. and Hashimi, N. H., Study of sub-surface sediments from northern Indian Ocean: oceanic responses to climatic changes. *J. Palaeontol. Soc. India*, 1994, **39**, 1–4.
22. Hays, J. D., Lozano, J. A., Shackleton, N. J. and Irving, G., An 18000 BP reconstruction of the Atlantic and western Indian sectors of the Antarctic Ocean. In *Investigations of Late Quaternary Paleo-oceanography and Paleo-climatology* (eds Cline, R. M. and Hays, J. D.), Geological Society of America, Memoirs, 1976, vol. 145, pp. 337–374.
23. Valsangkar, A. B., Kaisiddaiah, S. M. and Ambre, N. V., Geochemistry, factor analysis and clay mineral distribution of the sediments and relationship with the associated ferromanganese nodules from the SW Carlsberg Ridge. *Mahasagar*, 1992, **25**, 83–95.
24. Roberts, A. P. and Turner, G. M., Diagenetic formation of ferri-magnetic iron sulphide minerals in rapidly deposited marine sediments, New Zealand. *Earth Planet. Sci. Lett.*, 1993, **115**, 257–273.
25. Rutten, A. and De Lange, G. J., Sequential extraction of iron, manganese and related elements in S1 sapropel sediment, eastern Mediterranean. *Palaeogeogr., Palaeoclimatol., Palaeoecol.*, 2003, **190**, 79–101.
26. Froelich, P. N., Klinkhammer, G. P., Bender, M. L., Luedtke, N. A., Heath, G. R., Cullen, D. and Dauphin, P., Early oxidation of organic matter in pelagic sediments of the eastern equatorial Atlantic: suboxic diagenesis. *Geochim. Cosmochim. Acta*, 1979, **43**, 1075–1090.
27. Thomson, J., Higgs, N. C., Wilson, R. R. S., Croudace, I. W., de Lange, G. J. and van Santvoort, P. J. M., Redistribution and geochemical behaviour of redox-sensitive elements around S1, the most recent eastern Mediterranean sapropel. *Geochim. Cosmochim. Acta*, 1995, **59**, 3487–3501.
28. Reitz, A., Thomson, J., De Lange, G. J. and Hensen, C., Source and development of large manganese enrichments above eastern Mediterranean sapropel S1. *Palaeoceanography*, 2006, **21**, PA3007; doi:10.1029/2005PA001169.
29. Plueger, W. L., Friedrich, G. and Stoffers, P., Environmental controls on the formation of deep-sea ferromanganese concretions. *Monographs Series on Mineral Deposits*, Gebruder Borntraeger, Berlin, 1985, vol. 25, pp. 31–52.
30. Sundby, B., Transient state diagenesis in continental margin muds. *Mar. Chem.*, 2006, **102**, 2–12; doi:10.1016/j.archem.2005.09.016.

ACKNOWLEDGEMENTS. Part of the work was carried out under the CSIR Network Program on RIDGE (COR0006). We thank the DOD, New Delhi (now MoES) for ship time. We also thank the officers and crew of *ORV Sagar Kanya* for their skillful operations and the shipboard scientific and technical party for support in sample and data collection during SK-114, SK-154 and SK-207 cruises. A.B.V. is grateful to Prof. R. Shankar, Mangalore University for carrying out MS measurements on sub-sections. We thank Prof. D. Chandrasekhar, IIT Bombay for helpful comments on the manuscript. Technical support given by G. A. Prabhu for XRD, S. Vijayan during geochronological analysis and P. Pawaskar in preparing the figures is acknowledged. This is NIO contribution no. 4516.

Received 1 September 2008; revised accepted 2 March 2009